P43   MEASUREMENTS OF DSD SECOND MOMENT BASED ON LASER EXTINCTION

John E. Lane*
Easi-ESC, Kennedy Space Center, FL, USA
Linwood Jones
University of Central Florida, Orlando, FL, USA
Takis C. Kasparis
Cyprus University of Technology, Lemesos, Cyprus
Philip Metzger
NASA, Kennedy Space Center, FL, USA

ABSTRACT

Using a technique recently developed for estimating the density of surface dust dispersed during a rocket landing, measuring the extinction of a laser passing through rain (or dust in the rocket case) yields an estimate of the 2nd moment of the particle cloud, and rainfall drop size distribution (DSD) in the terrestrial meteorological case. With the exception of disdrometers, instruments that measure rainfall make indirect measurements of the DSD. Most common of these instruments are the rainfall rate gauge, measuring the $11/3^{th}$ moment, (when using a $D^{2/3}$ dependency on terminal velocity). Instruments that scatter microwaves off of hydrometeors, such as the WSR-88D, vertical wind profilers, and microwave disdrometers, measure the 6th moment of the DSD. By projecting a laser onto a target, changes in brightness of the laser spot against the target background during rain, yield a measurement of the DSD 2nd moment, using the Beer-Lambert law. In order to detect the laser attenuation within the 8-bit resolution of most camera image arrays, a minimum path length is required, depending on the intensity of the rainfall rate. For moderate to heavy rainfall, a laser path length of 100 m is sufficient to measure variations in optical extinction using a digital camera. A photo-detector could replace the camera, for automated installations. In order to spatially correlate the 2nd moment measurements to a collocated disdrometer or tipping bucket, the laser's beam path can be reflected multiple times using mirrors to restrict the spatial extent of the measurement. In cases where a disdrometer is not available, complete DSD estimates can be produced by parametric fitting of DSD model to the 2nd moment data in conjunction with tipping bucket data. In cases where a disdrometer is collocated, the laser extinction technique may yield a significant improvement to in-situ disdrometer validation and calibration strategies.

1. BACKGROUND

The origins of this work started with the need to determine and quantify damage that could be done by robotic landers getting too close to the Apollo landing sites. Data has shown that dust and soil particles

Corresponding author address: Easi-ESC, MS: ESC-58, Kennedy Space Center, FL 32899, 321-867-6939; e-mail: John.E.Lane@nasa.gov.

thrown up by the rocket exhaust of a lander could sand blast delicate hardware in the vicinity. Such impacts to those materials could ruin their scientific value in answering the question of what happens to manmade materials left in a lunar environment for 40 years (Immer, 2011).
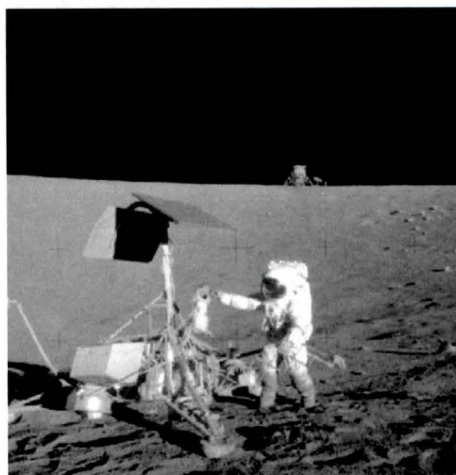

Figure 1: November 1969 - Allan Bean examining Surveyor III. Note Apollo 12 LM in background.

1.1 Apollo 12 and Surveyor III

Apollo 12 astronauts, Pete Conrad and Al Bean returned pieces of the Surveyor III spacecraft which received damage from plume propelled regolith dust particles. The Surveyor III lander, a robotic craft that touched down on the moon two years before Apollo 12, is located 155 m from the lunar module "Intrepid" (see Figure 1). The astronauts walked over to the Surveyor to find it was covered in moon dust even though it was largely protected from the blast by a crater. Plans have been proposed to mount a laser sensor and camera package (*Plume Erosion Sensor*) on the bottom of one of the landers taking part in the Google X-Prize competition, as a NASA payload. The sensor should be able to pick up the blowing dust and soil, providing critical data to verify and calibrate plume erosion models. This will also help formulate operational guidelines for other landers such as how far away from the Apollo sites new landers can touch down without risking damage to the Apollo descent module and other adjacent historical hardware.
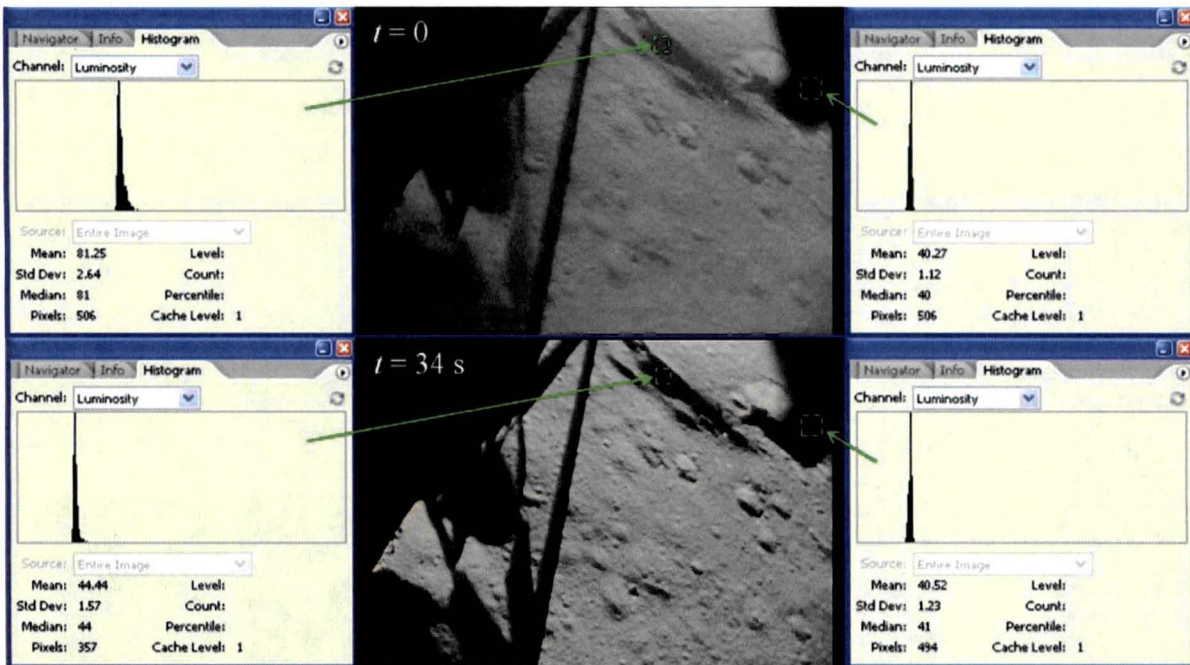
Figure 2. Luminosity measurements of Apollo 14 landing videos following engine cutoff.
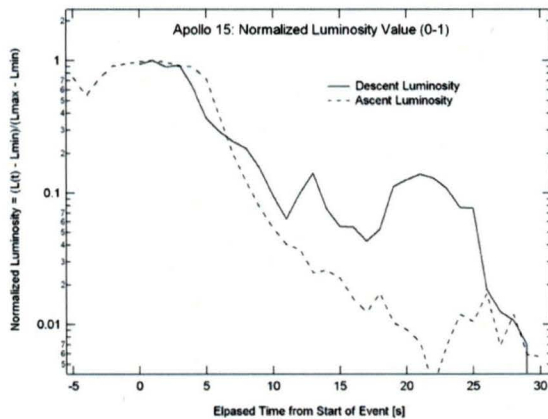

Figure 3. Luminosity measurements of Apollo 14 landing and ascent videos.

1.2 Apollo 14 Dust Clearing

Figure 2 shows the view from the LM right cockpit window during landing of Apollo 14. By measuring the luminosity of key areas of the video image sequence, a plot of the relative dust density versus time is produced, as shown in Figure 3 for both descent and ascent. In this analysis it can be observed that clearing rates are indicative of similar physical mechanisms, such as rocket induced electrostatic levitation. This analysis can provide valuable information on the dust density and clearing properties of the lunar surface after engine shutdown. However, a difficulty with this approach is that the ambient lighting (from the sun) is not uniform or necessarily predicable.

1.3 Plume Erosion Sensor (PES)

A improvement to the previous analysis is to use a laser to provides a calibrated light source that can be modulated so that the brightness of scattered and/or transmitted light can be detected using commercial off-the-shelf (COTS) video camera and custom image processing software, allowing optical density and thus plume erosion rate to be measured (see Figure 4). Using a small, light-weight COTS laser will make the mass of the instrument extraordinarily small. The laser can be turned on and off, allowing calibration of the unknowns of the scattered background light as well as those of the video camera.

By having a baseline between the lasers and the camera, observations can be made of not only the spot of light reflected off the lunar surface (transmitted through the cloud twice, measuring only vertically integrated optical density), but also the light side-scattered from the beam as it transmits through the surface. This provides a measure of dust density versus height in the cloud and thus may enable us to decorrelate shear stress from rarefaction as the two independent variables in lunar soil erosion. That is because higher particles in the cloud generally eroded from closer to the lander and have had more time to rise to those heights, whereas lower particles eroded from locations further away and have had less time to lift any higher. Particles at closer locations are subjected to less rarefied gas than those farther away. As the lander descends, the shear stress

changes relative to the zones of rarefaction. Thus, by measuring optical density at various heights in the cloud during descent, we obtain a 2-dimensional array of parameters corresponding to variation of both rarefaction and shear stress somewhat independently.
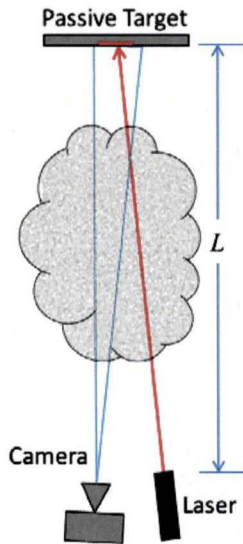

Figure 4. PES configuration.

Conceptually, the Plume Erosion Sensor (PES) attempts to derive microphysical properties of plumes of lunar dust from images taken during landing. The cameras will record images of a dust plume intersecting the path of the laser and the intensity of both reflected and scattered light will be analyzed and used to derive particle density, which is needed for accurately estimating erosion rates of lunar regolith.

1.4 Laboratory Simulations

A prototype PES was fabricated using a COTS laser and camera. The laser was Class II red (640 nm), 1 mW Stocker-Yale laser pointer. The camera was a Nikon D80 SLR. Two configurations were tested, as shown in Figure 5. Configuration-1 is the "side scatter" case, where the laser and camera can be at any arbitrary angle and not limited to the orthogonal alignment shown in Figure 5. Figure 6 shows the dust transport simulation chamber and laser dust density measurement, corresponding to configuration-1 (laser side-scatter measurement). Figure 7 is the dust chamber configured with the configuration-2 (laser spot measurement).

The laboratory dust simulations of the lunar environment is lunar simulant (JSC-1a), is a good example of creating an analog which is more convenient (so far it has been difficult to get back to the moon to do experiments). Another analog is using hydrometeors to replace the dust particles.
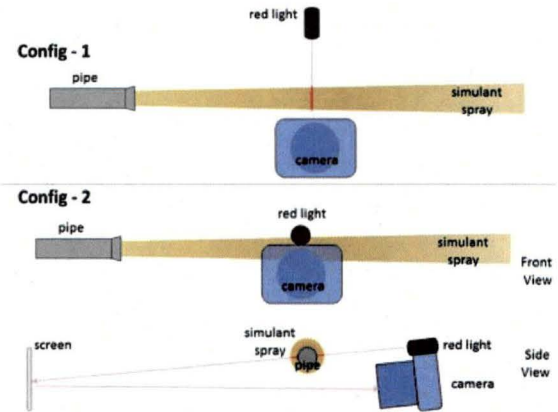

Figure 5. Laboratory laser dust density measurement.

Figure 6. Laboratory laser dust density measurement, corresponding to configuration -1
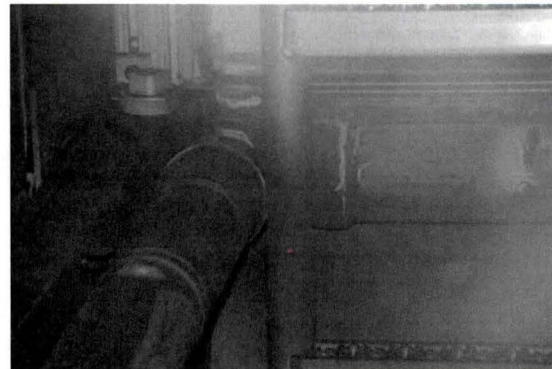

Figure 7. Laboratory laser dust density measurement, corresponding to configuration-2.
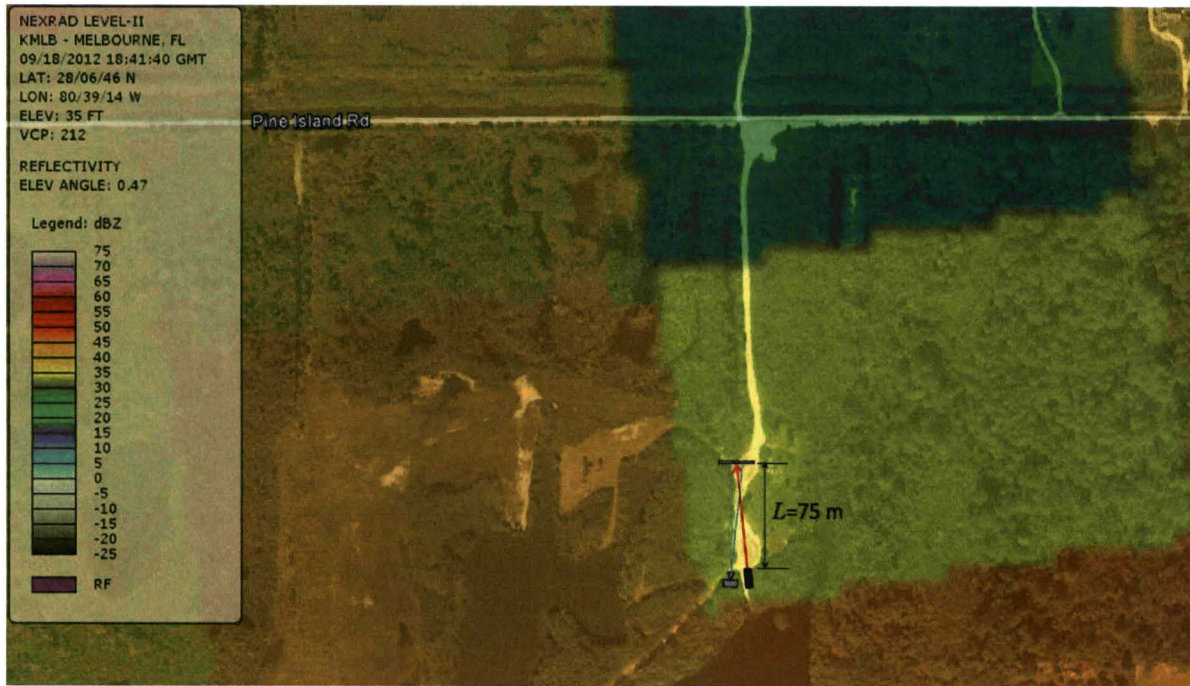
Figure 8. PES with 75 m distance to passive target, overlaid with September 18, 2012 Melbourne NEXRAD super-resolution data (250 m × 0.5°).

2. A PES BASED TRANSMISSOMETER

The basic configuration of the PES for hydrometeor applications again consists of a single laser and a digital camera. The camera is mounted near the laser as shown in Figure 4. Typically, the laser projection distance is several to tens of meters (~75 m for the terrestrial atmospheric application). A laser spot on the surface (in the lunar implementation) is imaged with the camera. Image processing algorithms find the laser spot, average the brightness over the spot, and also measure background intensity to either side of the laser spot. Digital signal processing of these measurements provide an estimate of the 2nd moment of the size distribution of particles traversed by the laser.

Table 1. Optical 2nd Moment Experiment Matrix

	Granular Materials	Hydrometeors
Side-Scatter Extinction	JSC-1a lunar simulant	*future work?*
Laser Spot Extinction	JSC-1a lunar simulant	rain DSD

Table 1 summarizes the two PES configurations for measuring particle density. The side-scatter configuration (*Config-1* of Figure 5) is shown in Figure 9 where the scattered light from the laser is mapped onto the camera's image array. This method has not yet been tried with rain, but will be a likely area of future work. *Config-2* of Figure 5 is the "spot" measurement, used in Figures 7 and 8.
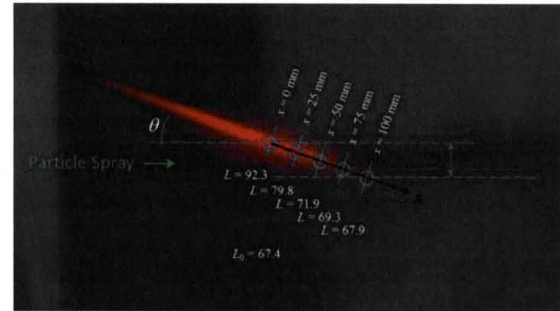

Figure 9. Side scatter measurements through lunar dust simulant.

2.1 Hydrometeor DSD Quantities

Recall that the x-moment of a distribution is defined as:

$$M_x = \int_0^\infty D^x N(D)dD \qquad (1)$$

$N(D)$ is the drop size distribution (DSD). For $N(D)$ equal to an exponential DSD (Marshall-Palmer DSD is a special case of the exponential function):

$$M_x = N_0 \int_0^\infty D^x e^{-D/D_0} dD \qquad (2)$$
$$= N_0 D_0^{x+1} \, \Gamma(x+1)$$

where $\Gamma(x)$ is the Gamma function. If $N(D)$ is modeled as a gamma DSD:

$$M_x = N_0 \int_0^\infty D^{x+\gamma} e^{-D/D_0} dD \qquad (3)$$
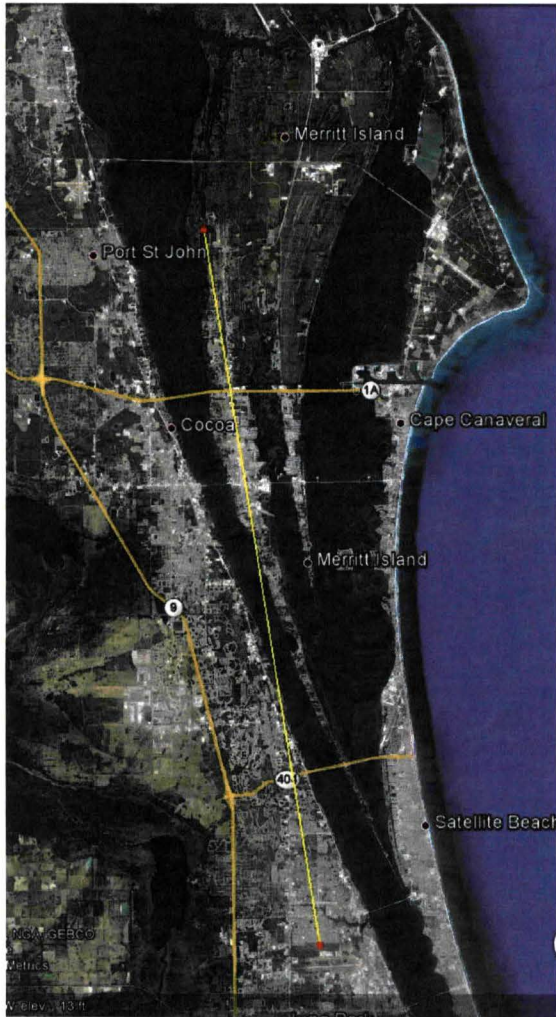$$= N_0 D_0^{x+\gamma+1} \, \Gamma(x+\gamma+1)$$

Figure 10. Yellow diagonal line connects radar site at Melbourne airport (red square at bottom) to the DSD site depicted in Figure 8, red square in upper portion of figure. The distance is $r = 42.3$ km.

The quantity measured and reported by weather radar is the 6th moment of the drop size distribution:

$$M_6 = N_0 \int_0^\infty D^{6+\gamma} e^{-D/D_0} dD \qquad (4)$$
$$= N_0 D_0^{6+\gamma+1} \, \Gamma(6+\gamma+1)$$

where the above integral is evaluated for the ideal case of the gamma DSD. Radar reflectivity data Z is typically reported in units of dB ($dBZ \equiv 10 \log_{10} Z$). The 6th moment of the DSD can be simply expressed in the case of the exponential DSD ($\gamma = 0$):

$$Z = M_6 = N_0 \int_0^\infty D^6 e^{-D/D_0} dD$$
$$= N_0 D_0^7 \, \Gamma(7) \qquad (5)$$
$$= 720 \, N_0 \, D_0^7 \quad [\text{m}^{-3}\text{mm}^6]$$

The radar reflectivity, as described by Equation (5), corresponds to an average value throughout the volume scan bin. For the new super-resolution NEXRAD data, the sampling volume of a radar reflectivity bin is the range increment $\Delta r = 0.25$ km multiplied by the $\Delta\theta = 0.5°$ beam width:

$$V_r = \Delta r \, \pi (r\Delta\theta/2)^2 \qquad (6)$$

which equates to 0.027 km^3, at the Pine island site depicted in Figure 8. The sampling time of the radar corresponds to the volume scan rate which is roughly 5 min or 300 s.

Table 2. Sampling volume and rate comparison of DSD related instruments.

	Volume [m^3]	DSD Moment	$f = 1/T$ [s^{-1}]	DSD Qty
NEXRAD (super-res)	~3×10^7 *	6	~1/300	Z [m^{-3} mm^6]
Rain Gauge	$147/R$ **	~11/3	$R/914$	R [mm h^{-1}]
Disdro-meter	~1.5	-	~1/60	$H(D,t)$
Laser Extinction	~0.4 ***	2	30	β_r [km^{-1}]

* NEXRAD volume evaluated at $r = 42.3$ km
** Evaluated for 8 in diameter opening and 0.01 in tip
*** Evaluated for 75 m range and 1 mrad divergence

A rain gauge sampling volume corresponds to the product of sampling area at the bucket opening ($A = 8$ [in] is a typical diameter) and the distance rain travels between tips of the bucket. The sampling time T is variable and is equal to the effective collector depth ($h_0 = 0.01$ [in] in most cases) divided by the rainfall rate R: $T = h_0/R$. The maximum rate is limited by the filling time of the tipping bucket collector. The gauge

volume is then $V_G = ATv_T \approx 5A/f = 147/R$, where an average drop terminal velocity, $v_T = 5$ m/s is assumed.

The sampling volume of the disdrometer, like the rain gauge, is estimated as the collection area (50 cm^2 is a typical area) times the distance drops travel to reach the collection area. The sampling period of the disdrometer is usually set in software and a value of $T = 60$ s is typical. The corresponding sampling volume $V_D = ATv_T \approx 300A = 1.5$ m^3, where an average drop terminal velocity, $v_D = 5$ m/s is again assumed. These values are summarized in Table 2.

The quantity measured and reported by a rainfall rate gauge, such as a tipping bucket, is approximately the $x = 3 + \beta_v$ moment of the drop size distribution:

$$M_{3+\beta_v} = \int_0^\infty D^{\beta_v} D^3 N(D)\, dD$$
$$= N_0 \int_0^\infty D^{3+\beta_v+\gamma} e^{-D/D_0}\, dD \quad , \tag{6}$$
$$= N_0 D_0^{3+\beta_v+\gamma+1}\, \Gamma(4+\beta_v+\gamma)$$

where the above integral is evaluated for the ideal case of the gamma DSD. The parameter $\beta_v = 2/3$ describes an approximation to the drop terminal velocity, $v(D)$:

$$v(D) \approx \alpha_v D^{\beta_v} \quad , \tag{7}$$

where $\alpha_v = 3.778$ [m·s^{-1}·mm$^{-2/3}$] (Ulbrich, 1977). The 6th moment of the DSD can be simply expressed in the case of the exponential DSD ($\gamma = 0$):

$$M_{11/3} = N_0 D_0^{14/3}\, \Gamma(14/3)$$
$$= 14.711\, N_0 D_0^{14/3} \quad . \tag{8}$$

Rainfall rate R is the integral over the product of the drop size distribution and the drop volume, modified by the drop terminal velocity:

$$R = \int_0^\infty \tfrac{\pi}{6} D^3 v(D) N(D)\, dD \quad . \tag{9}$$

The rainfall rate of Equation (9) is not in standard units of [mm h^{-1}], so it needs to be modified by the number of (3600 s)/h, ((0.001 m)/mm)^3, and (1000 mm)/m:

$$R = 3600 \cdot (10^{-3})^3 \tfrac{\pi}{6} \int_0^\infty D^3 v(D) N(D)\, dD \cdot 1000 \quad . \tag{10}$$
$$= \frac{3\pi\alpha_v}{5000} M_{11/3}$$

Equation (10) can be further simplified if making the assumption that $N(D)$ is described by an exponential distribution:

$$R = \frac{3\pi\alpha_v}{5000} \Gamma(14/3) N_0 D_0^{14/3} \quad . \tag{11}$$
$$= 0.1048\, N_0 D_0^{14/3} \quad [\text{mm h}^{-1}]$$

If Equations (5) and (11) are combined, eliminating D_0, then Z can be expressed in terms of R:

$$Z = 21222.2\, N_0^{-1/2} R^{3/2} \quad . \tag{12}$$

If the Marshall-Palmer value of $N_0 = 8000$ [m^{-3} mm^{-1}] is used, the Z-R relationship becomes:

$$Z = 237.3\, R^{3/2} \quad . \tag{13}$$

The Marshall-Palmer Z-R is $Z = 200R^{1.6}$, while the NWS convective Z-R is $Z = 300R^{1.4}$. The Z-R relationship of Equation (13) is self-consistent, based on the terminal velocity formula shown in Equation (7).

The quantity measured by the PES is the optical extinction coefficient for rain β_r [km^{-1}]. The optical extinction coefficient is equal to the 2nd moment of the DSD modified by the extinction efficiency, Q_e:

$$\beta_r = Q_e \tfrac{\pi}{4} M_2$$
$$= Q_e \tfrac{\pi}{4} \int_0^\infty D^2 N(D)\, dD \quad . \tag{14}$$

The factor of $\pi/4$ is included since the scattering cross-sectional area of the particle is needed. If an exponential DSD is assumed, then Equation (14) becomes:

$$\beta_r = Q_e \tfrac{\pi}{4} M_2$$
$$= Q_e \tfrac{\pi}{4} \Gamma(3) D_0^3 N_0 \quad . \tag{15}$$

The units of Equation (15) are not correct (we are defining the extinction coefficient in units of m^{-1}).

$$\beta_r = Q_e \tfrac{\pi}{4} (10^{-3})^2 \Gamma(3) D_0^3 N_0$$
$$= \frac{\pi}{2 \cdot 10^6} Q_e\, D_0^3 N_0 \quad [\text{m}^{-1}] \tag{16}$$

In precisely the same way that weather radar relates reflectivity (reflected scattering of microwaves) to rainfall rate, using the Z-R relationship, a similar β_r-R relation can be derived to estimate optical extinction in terms of rainfall rate (Atlas, 1953; Bhattacharyya, 2000; Grabner, 2011; Uijlenhoet, 2011) by combining Equations (5) and (17) and elimination D_0:

$$\beta_r = 6.698 \cdot 10^{-6} Q_e N_0^{5/14} R^{9/14} \quad [\text{m}^{-1}] \quad . \tag{17}$$

If the Marshall-Palmer $N_0 = 8000$ [m^{-3} mm^{-1}] is used and $Q_e = 2$, then the β_r-R relationship becomes:

$$\beta_r = 0.1659 Q_e\, R^{9/14} \quad [\text{km}^{-1}]$$
$$= 0.3318 R^{9/14} \quad . \tag{18}$$

The PES instrument when in the "extinction spot" mode is similar in principle to the RVR transmissometer, where the main difference is that the PES uses a digital camera on the same side as the laser source in place of the transmissometer's sensor. The PES target is then a just a simple passive reflector.

3. SEPTEMBER 18, 2012 DATA

The data set for this day consists of NEXRAD Level II reflectivity at the lowest scan elevation angle, with laser extinction data. A green 5 mW laser with approximately 1 mrad divergence produced an 8 cm spot on the passive target. The camera used to acquire the laser spot images in Figure 11 was a Nikon D60 with a 500 mm fixed focal length lens, with manual focus and aperture.

A tipping bucket rain gauge and an accumulation gauge were also part of the set of instruments used during this rain event.

Figure 11 is a decomposition of a camera image frame before the start of rain. The top left shows the original color image of the laser spot. The next three blocks show the decomposition of the color image into red, blue, and green components. The brightest one in the bottom right is the green component. This figure shows that the frequency of the green laser is conveniently well matched to the green channel of the camera. This provides a free boost to the signal to noise processing strategy by simply discarding the red and blue components. The bottom two graphs in Figure 11 are 3D surface plots of the green image component. It is this that is processed, averaged, with background removal to obtain the measured value of optical extinction.
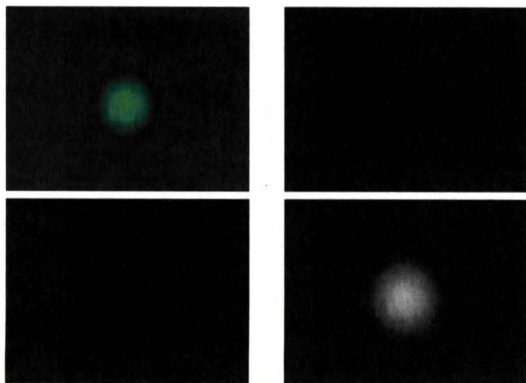

Figure 11. No rain case: Top left – original color image of laser spot; top right – blue component of image; middle left – red component; middle right – green component; bottom two – 3D surface plot of green component.
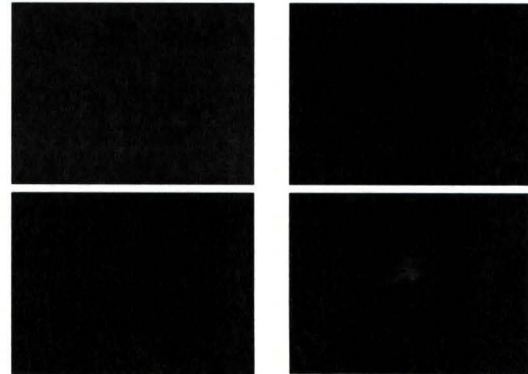

Figure 12. Heavy rain case: Top left – original color image of laser spot; top right – blue component of image; middle left – red component; middle right – green component; bottom two – 3D surface plot of green component.

Figure 12 is the corresponding laser-camera image data during heavy rain (see Figure 8), with a radar Z value of approximately 40 dBZ over the laser site. The complete data set for this rainfall event is shown in Figure 13. The optical extinction coefficient is plotted as the negative of the natural logarithm of the luminosity of the green channel, minus the average background, all normalized to one, divided by the distance between laser and camera:

$$\beta_r = -\frac{1}{x}\log\left(\frac{I_0 - I_b}{(I_0 - I_b)_{max}}\right) \quad [km^{-1}] \quad , \quad (18)$$

where I_0 is the average intensity of the green channel over the spot, I_b is the average green channel background and x is the round trip distance between laser and camera (x = 150 m, as shown in Figure 8).
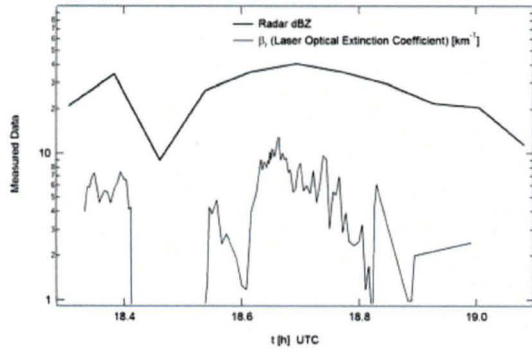

Figure 13. September 18, 2012 rainfall event at Pine Island, FL. Normal width line is optical extinction coefficient measured by laser system; bold line is the average of nearest four bins of radar reflectivity from Melbourne NEXRAD (lowest elevation scan) over the laser site shown in Figure 8.

If an exponential DSD is assumed, the parameters N_0 and D_0, as well as Q_e can be found by combining $Z(t)$ and $\beta_r(t)$ for a complete rainfall event. The total accumulated gauge rainfall amount is also needed (the rainfall rate $R(t)$ is not required).

$$R_\beta = \alpha_\beta N_0^{-5/9} Q_e^{-14/9} \beta_r^{14/9} \quad . \quad (19)$$

where $\alpha_\beta \equiv 1.118 \times 10^8$.

$$R_T = \sum_n R_\beta(n)\Delta t_n \quad (20)$$
$$= \alpha_\beta N_0^{-5/9} Q_e^{-14/9} \Psi_\beta$$

where,

$$\Psi_\beta \equiv \sum_n \beta_r^{14/9}(n)\Delta t_n \quad . \quad (21)$$

Following the same procedure for the radar computed rainfall rate form Equation 12):

$$R_Z = \alpha_Z N_0^{1/3} Z^{2/3} \quad . \quad (22)$$

where $\alpha_Z \equiv 1.304 \times 10^{-3}$.

$$R_T = \sum_n R_Z(n)\Delta t_n \quad (23)$$
$$= \alpha_Z N_0^{1/3} \Psi_Z$$

where,

$$\Psi_Z \equiv \sum_n Z^{2/3}(n)\Delta t_n \quad . \quad (24)$$

Equating Equations (20) and (23) and solving for N_0, results in:

$$N_0 = \left(\frac{\alpha_\beta}{\alpha_Z} \cdot \frac{\Psi_\beta}{\Psi_Z}\right)^{9/8} Q_e^{-7/4} \quad . \quad (25)$$

Substituting Equation (25) into (20) or (23) and solving for Q_e gives:

$$Q_e = \left(\frac{\alpha_Z \Psi_Z}{R_T}\left(\frac{\alpha_\beta \Psi_\beta}{\alpha_Z \Psi_Z}\right)^{3/8}\right)^{12/7}$$
$$= \left(\frac{\alpha_\beta \Psi_\beta}{R_T}\left(\frac{\alpha_Z \Psi_Z}{\alpha_\beta \Psi_\beta}\right)^{5/8}\right)^{12/7} \quad (26)$$

Using N_0 = 147381 $m^{-3}mm^{-1}$ and Q_e = 1.81 from evaluation of Equations (25) and (26) for the September 18 data, Equations (5) and (16) can be inverted to solve for D_0. R_T as measured by an accumulation rain gauge was equal to 7.6 mm for the September 18 event. D_0 is plotted in Figure 14 for radar reflectivity and laser extinction cases. Note that scattering theory predicts that Q_e = 2 for typical raindrop sizes and optical wavelength waves (Berg, 2011). The 10% deviation of Q_e using Equation (26) from 2, is due to the accumulation of many error sources throughout the measurement and analysis process. These errors will be discussed in the Summary Section.
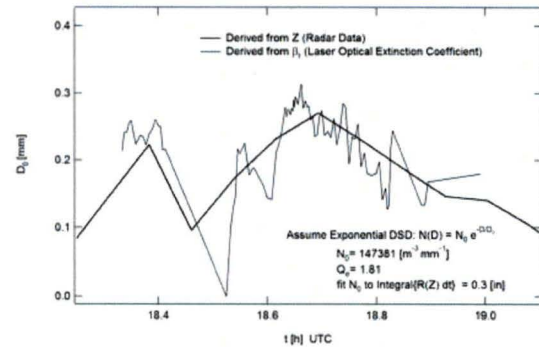

Figure 14. D_0 obtained from inverting Equations (5) and (16), using N_0 = 147381 $m^{-3}mm^{-1}$ and Q_e = 1.81.

The radar predicted rainfall rate can be computed from the radar reflectivity Z by inverting Equation (12) and solving for R. Similarly, the laser extinction β_r rainfall rate can be computed by inverting Equation (17) and solving for R. The rainfall rates derived from Z and β_r are plotted in Figure 15. Note that these two plots are not independent since the parameters of the exponential DSD were derived from Equations (25) and (26) which couples both measurements.
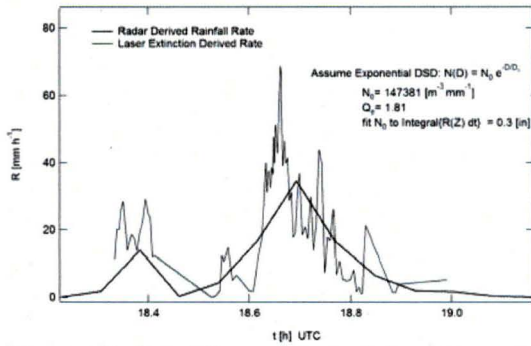

Figure 15. Rainfall rates derived from Z and β_r, using $N_0 = 147381\ m^{-3}mm^{-1}$ and $Q_e = 1.81$.

4. OCTOBER 2, 2012 DATA

The same location at Pine Island as shown in Figure 8 was used on October 2, 2012. The overall conditions were similar. Again, the dataset for this rainfall event consisted of NEXRAD Level II reflectivity at the lowest scan elevation angle, with laser extinction data. The same green 5 mW laser with 1 mrad divergence was used, producing an 8 cm spot on the passive target. The same Nikon D60 with a 500 mm fixed focal length lens was used. A tipping bucket acquired rainfall rate and an accumulation rain gauge measured the total rainfall amount.
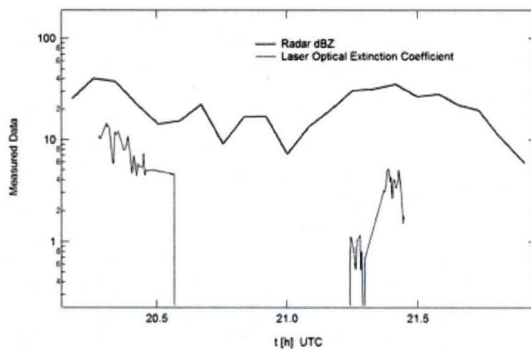

Figure 16. October 2, 2012 rainfall event at Pine Island, FL. Normal width line is the optical extinction coefficient measured by the laser system; bold line is the average of the nearest four bins of radar reflectivity from Melbourne NEXRAD (lowest elevation scan) over the laser site shown in Figure 8.

Using the image processing algorithm summarized by Equation (18), along with the laser spot location, averaging, and background measurement processing, the camera image sequence was converted to an optical extinction coefficient versus time. This measurement along with the NEXRAD data from the NCDC archive, is plotted in Figure 16.
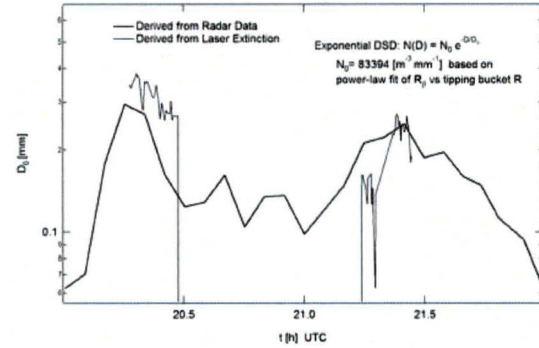

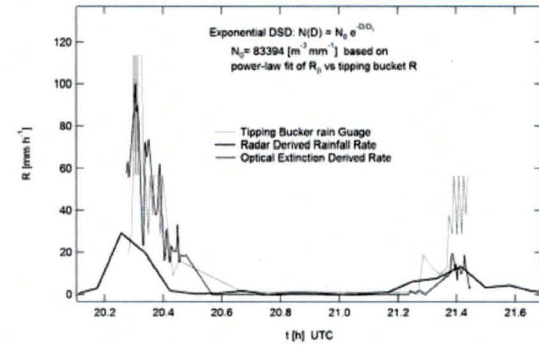Figure 17. D_0 obtained from inverting Equations (5) and (16), using $N_0 = 83394\ m^{-3}mm^{-1}$ and $Q_e = 2$.

Figure 18. Rainfall rates derived from Z and β_r, using $N_0 = 83394\ m^{-3}mm^{-1}$ and $Q_e = 2$.

A different approach was used to analyze the October 2 data, since tipping bucket rainfall rate data was available, unlike the September 18 event. Solving Equation (17) for R, results in an optical extinction estimated rainfall rate, R_β. If a scatter plot is produced of tipping bucket rainfall rate versus the optical extinction coefficient, the slope of a straight line fit on a log-log plot should be 14/9, if an exponential DSD is used. Note that if a gamma distribution is used, where $N(D)$ is defined as:

$$N(D) = N_0\, D^\mu e^{-D/D_0} \qquad , \qquad (27)$$

the resulting slope of the curve is:

$$slope = \frac{d(\log R_\beta)}{d(\log \beta_r)} = \frac{14/3 + \mu}{3 + \mu} \qquad . \qquad (28)$$

Following this procedure, a value of $\mu = 0$ was finally used for this dataset, since due to the low fidelity of the scatter plot, a particular γ was not favored. Some of the reasons for this will be discussed in the Summary section.

The scatter plot fit of tipping R versus optical extinction on a log-log plot with $\mu = 0$ results in the following:

$$\log R_\beta = \log\left(\frac{1.118 \times 10^8}{N_0^{5/9} Q_e^{14/9}}\right) + \left(\tfrac{14}{9}\right) \log \beta_r \quad \cdot \quad (28)$$

The value of N_0 can then be found from the intercept, first term on RHS of Equation (28), and using the expected value of the efficiency factor, $Q_e = 2$. Following this procedure for the October 2 dataset, $N_0 = 83394$ m^{-3}mm^{-1} with $\mu = 0$. Now the D_0 and R can be computed and plotted (see Figures 17 and 18). Note a full treatment of the gamma DSD will require re-deriving most of the previous equations from the beginning. It is not that difficult, but the math is messier and does not reveal anything that the exponential DSD doesn't show. However, in the case of higher fidelity scatter plot data of rain gauge versus optical extinction, the value of γ should be apparent.

5. SUMMARY AND DISCUSSION

There are at least two primary error sources that can be identified affecting the accuracy of the analysis described above. The first and most difficult to deal with is due to the vast differences in spatial and temporal sampling size associated with various rainfall measurement instruments. Table 2 is an attempt at capturing and quantifying these differences for comparison. The spatial and temporal sampling of NEXRAD is different by orders of magnitude when compared to a rain gauge. This is one advantage of using rain gauge and a collocated laser extinction measurement, since both operate in similar volume and time scales. (Note that in Table 2, the rain gauge and disdrometer sample volumes are computed as the sensing area times the distance rain falls during a sample interval). Therefore, the differences in NEXRAD sampling volume and rates in the September 18 dataset is a reasonable explanation for the deviation of the predicted extinction efficiency factor from its ideal value of $Q_e = 2$.

The laser and rain gauge data agree reasonably well in the October 2 dataset, but again the NEXRAD is significantly off from the rain gauge data. The second rain event in Figure 18, starting around 21:15, shows a significant mismatch between the laser and rain gauge. This may be explained by a voltage change in the laser mechanism leading to an unexpected intensity change in the laser spot. Another possible explanation is that the spatial variability of rain over the laser distance (75 m) was unusually high (the *raining on one side of the street and not the other*

scenario). However, there is no way to confirm this hypothesis.

Another point that should be discussed is why make the laser 2nd moment measurements to start with. What can it provide that NEXRAD, rain gauges, and disdrometers don't provide. There are several answers to that.

The first benefit from a collocated laser extinction measurement is to provide new data for disdrometer in situ calibration. In situ calibration of disdrometers is not a commonly used technique, but previous research (Kasparis, 2010) demonstrates that it is one of the best strategies leading towards implementing and deployment of lower cost disdrometers. Lower cost disdrometers then translates into more disdrometers per research project to study spatial and temporal variability of the rainfall DSD.

Another benefit of using the 2nd moment measurement of the local DSD is to provide additional data to a 3D-DSD model (Lane, 2009). The ultimate description of rainfall is in terms of a DSD as a function of x, y, z, and t: $N(D;x,y,z,t)$. In this sense, the 3D-DSD uses all available data, including NEXRAD, rain gauges, disdrometers, and optical extinction, as well as wind data.

A future area of research is to extend the "side-scatter" technique to hydrometeor measurements. In this way, the functionality of weather Lidar (Shipley, 1974) is approached with the capability of spatial measurement of extinction along the laser beam path. This technique was developed and tested for the dust density measurement case (see Figure 9), under very ideal conditions. The next step is to see if it could be extended to the general DSD case.

6. REFERENCES

Atlas, D., 1953: Optical extinction by rainfall. *Journal of Atmospheric Sciences*, **10**, 486-486.

Berg, M.J., C.M. Sorensen, and A. Chakrabarti, 2011: A new explanation of the extinction paradox, *Journal of Quantitative Spectroscopy and Radiative Transfer*, **112**(7), 1170-1181.

Bhattacharyya, S., Dan, M., and A. K. Sen, 2000: Modelling of drop size distribution of rain from rain rate and attenuation measurements at millimeter and optical wavelengths. *International Journal of Infrared and Millimeter Waves*, **21**(12), 2065-2075.

Grabner, Martin, and Vaclav Kvicera, 2011: Analysis of rain effect on free space optical and microwave communication links. *Telecommunications (ConTEL), Proceedings of the 2011 11th International Conference on*, pp. 185-188. IEEE.

Immer, C., J. Lane, P. Metzger, and S. Clements, 2011: Apollo video photogrammetry estimation of plume impingement effects. *Icarus*, **214**(1), 46-52.

Kasparis, T., J. Lane, and L. Jones, 2010, March:. Modeling of an impact transducer for in situ adaptive disdrometer calibration. In *Communications, Control and Signal Processing (ISCCSP), 2010 4th International Symposium on* (pp. 1-4). IEEE.

Lane, J. E., T. Kasparis, P. T. Metzger, and W. L. Jones, 2009: Spatial and Temporal Extrapolation of Disdrometer Size Distributions Based on a Lagrangian Trajectory Model of Falling Rain. *arXiv preprint arXiv:0906.1614.*

Shipley, S. T., E. W. Eloranta, and J. A. Weinman, 1974: Measurement of Rainfall Rates by Lidar. *J. Appl. Meteor.*, **13**, 800–807.

Uijlenhoet, R., Cohard, J. M., and M. Gosset, 2011: Path-average rainfall estimation from optical extinction measurements using a large-aperture scintillometer. *Journal of Hydrometeorology*, **12**(5), 955-972.

Ulbrich, C. W., abd D. Atlas, 1977: A method for measuring precipitation parameters using radar reflectivity and optical extinction. *Annals of Telecommunications*, **32**(11), 415-421.

Figure 19. Rainfall measurement test site on the roof of the Engineering Building, UCF, Orlando, FL. Far left is a Joss disdrometer; center and far right are dual-head experimental UCF disdrometers. The large cylinders are tipping buckets. The Joss and tipping buckets are courtesy of NASA Goddard Space Flight Center. In situ calibration of the UCF disdrometers has previously been accomplished via attached tipping buckets which are multiplexed with the disdrometer audio signal.